

an Isocarb common acid bath autocarbonate system at 90 °C at the University of California Davis.

Mg/Ca ratios were measured on foraminifera collected from the same population and size fraction that was used for the stable isotope analyses. Approximately 600 µg of material per sample (~55 shells) was cleaned for trace and minor element analysis<sup>5</sup>. Briefly, samples underwent a multi-step process consisting of initial rinses in ultrapure water, followed by treatments with hot reducing and oxidizing solutions, transfers into new acid-leached micro-centrifuge vials, and finally leaches with a dilute ultrapure acid solution. All sample cleaning was conducted in laminar flow benches under trace-metal-clean conditions. Samples were then dissolved and analysed on a Finnigan Element-2 ICPMS at the University of California Santa Barbara using established procedures<sup>5</sup>. A full suite of trace- and minor-element measurements were made on each sample including Ca, Mg, Sr, Na, Cd, Ba, La, Ce, Nd, Eu, Lu, U, Al, Mn and Fe.

Elemental ratios of Fe/Ca and Al/Ca were used to monitor cleaning efficacy. Analyses with anomalously high Fe/Ca or Al/Ca ratios and/or with recovery of less than 20% after cleaning were rejected. Although Fe/Ca ratios gradually increased with depth in both cores, Al/Ca ratios remained uniformly low, typically <7 µmol mol<sup>-1</sup> in ODP 999A and <14 µmol mol<sup>-1</sup> in VM28-122, indicating that Mg contamination associated with detrital sediment in cleaned samples was not an issue at either site. Although Fe/Ca and Mn/Ca were higher in VM28-122, Mg/Ca did not correlate with Fe/Ca, Al/Ca or Mn/Ca in either core, indicating that the mineral phases containing these metals in the cleaned samples did not affect Mg/Ca ratios in the foraminiferal calcite.

**Error analysis**

Analytical precision for the δ<sup>18</sup>O<sub>C</sub> measurements is better than ±0.06‰. The pooled standard deviation of replicate Mg/Ca analyses from ODP 999A was ±1.7% (1 s.d., d.f. = 110). The pooled standard deviation of replicate Mg/Ca analyses from VM28-122 was ±2.4% (1 s.d., d.f. = 129). The overall precision of replicates in this study is slightly better than other tropical cores (typically ~3%)<sup>5,20</sup>, most probably reflecting the stability of the water column in the Colombian basin through the last glacial cycle. Standard deviation for the δ<sup>18</sup>O<sub>SW</sub> residual was calculated to be ± 0.2‰, using Monte Carlo methodology that assumed a 1σ normal distribution in the δ<sup>18</sup>O<sub>C</sub> and Mg/Ca measurements and in the Mg/Ca–SST and δ<sup>18</sup>O–SST calibrations.

Received 24 October 2003; accepted 19 January 2004; doi:10.1038/nature02346.

1. Boyle, E. A. Is ocean thermohaline circulation linked to abrupt stadial/interstadial transitions? *Quat. Sci. Rev.* **19**, 255–272 (2000).
2. Broecker, W. S., Bond, G., Klas, M., Bonani, G. & Wolfl, W. A salt oscillator in the glacial Atlantic? The concept. *Paleoceanography* **5**, 469–478 (1990).
3. Keigwin, L. D. & Boyle, E. A. Surface and deep ocean variability in the northern Sargasso Sea during marine isotope stage 3. *Paleoceanography* **14**, 164–170 (1999).
4. Duplessy, J. C. *et al.* Changes in surface salinity of the North Atlantic Ocean during the last deglaciation. *Nature* **358**, 485–488 (1992).
5. Lea, D. W., Pak, D. K. & Spero, H. J. Climate impact of Late Quaternary equatorial Pacific sea surface temperature variations. *Science* **289**, 1719–1724 (2000).
6. Elderfield, H. & Ganssen, G. Past temperature and δ<sup>18</sup>O of surface ocean waters inferred from foraminiferal Mg/Ca ratios. *Nature* **405**, 442–445 (2000).
7. Curry, W. B. & Oppo, D. W. Synchronous high-frequency oscillations in tropical sea surface temperatures and North Atlantic deep water production during the last glacial cycle. *Paleoceanography* **12**, 1–14 (1997).
8. Johns, W. E., Townsend, T. L., Fratantoni, D. M. & Wilson, W. D. On the Atlantic inflow to the Caribbean Sea. *Deep-Sea Res.* **1** **49**, 211–243 (2002).
9. Broecker, W. S., Peng, T. H., Jouzel, J. & Russell, G. The magnitude of global fresh-water transports of importance to ocean circulation. *Clim. Dyn.* **4**, 73–79 (1990).
10. Craig, H. & Gordon, L. I. In *Stable Isotopes in Oceanographic Studies and Paleotemperatures* (ed. Tongiorgi, E.) 9–130 (CNR, Pisa, 1965).
11. Bassinot, F. C. *et al.* The astronomical theory of climate and the age of the Brunhes-Matuyama magnetic reversal. *Earth Planet. Sci. Lett.* **126**, 91–108 (1994).
12. Chappell, J. *et al.* Reconciliation of late Quaternary sea levels derived from coral terraces at Huon Peninsula with deep sea oxygen isotope records. *Earth Planet. Sci. Lett.* **141**, 227–236 (1996).
13. Dekens, P. S., Lea, D. W., Pak, D. K. & Spero, H. J. Core top calibration of Mg/Ca in tropical foraminifera: refining paleotemperature estimation. *Geochem. Geophys. Geosyst.* **3**, no. 1022 (2002).
14. Thunell, R., Tappa, E., Pride, C. & Kincaid, E. Sea-surface temperature anomalies associated with the 1997–1998 El Niño recorded in the oxygen isotope composition of planktonic foraminifera. *Geology* **27**, 843–846 (1999).
15. Waelbroeck, C. *et al.* Sea-level and deep water temperature changes derived from benthic foraminifera isotopic records. *Quat. Sci. Rev.* **21**, 295–305 (2002).
16. Ruhlemann, C., Mulitza, S., Muller, P. J., Wefer, G. & Zahn, R. Warming of the tropical Atlantic ocean and slowdown of thermohaline circulation during the last deglaciation. *Nature* **402**, 511–514 (1999).
17. Conkright, M. *et al.* *NODC Internal Report* at (<http://iridl.ldeo.columbia.edu/SOURCES/NOAA/NODC/WOA98/>) (NODC, Silver Springs, Maryland, 1998).
18. Hastings, D. W., Russell, A. D. & Emerson, S. R. Foraminiferal magnesium in *Globigerinoides sacculifer* as a paleotemperature proxy. *Paleoceanography* **13**, 161–169 (1998).
19. Grootes, P. M. & Stuiver, M. Oxygen 18/16 variability in Greenland snow and ice with 10<sup>3</sup> to 10<sup>5</sup>-year time resolution. *J. Geophys. Res.* **102**, 26455–26470 (1997).
20. Lea, D. W., Pak, D. K., Peterson, L. C. & Hughen, K. A. Synchronicity of tropical high latitude Atlantic temperatures over the last glacial termination. *Science* **301**, 1361–1364 (2003).
21. Vink, A. *et al.* Shifts in the position of the North Equatorial Current and rapid productivity changes in the western Tropical Atlantic during the last glacial. *Paleoceanography* **16**, 1–12 (2001).
22. Watanabe, T. A., Winter, A. & Oba, T. Seasonal changes in sea surface temperature and salinity during the Little Ice Age in the Caribbean Sea deduced from Mg/Ca and 18O/16O ratios in corals. *Mar. Geol.* **173**, 21–35 (2001).
23. Jouzel, J., Hoffmann, G., Koster, R. D. & Masson, V. Water isotopes in precipitation: data/model comparison for present-day and past climates. *Quat. Sci. Rev.* **19**, 363–379 (2000).

24. Dürkoop, A., Hale, W., Mulitza, S., Patzold, J. & Wefer, G. Late Quaternary variations of sea surface salinity and temperature in the western tropical Atlantic: Evidence from δ<sup>18</sup>O of *Globigerinoides sacculifer*. *Paleoceanography* **12**, 764–772 (1997).
25. Stidd, C. K. The use of eigenvectors for climate estimates. *J. Appl. Meteorit.* **6**, 255–264 (1967).
26. Vellinga, M. & Wood, R. A. Global climatic impacts of a collapse of the Atlantic thermohaline circulation. *Clim. Change* **54**, 251–267 (2002).
27. Peterson, L. C., Haug, G. H., Hughen, K. A. & Rohl, U. Rapid changes in the hydrologic cycle of the tropical Atlantic during the last Glacial. *Science* **290**, 1947–1951 (2000).
28. Lynch-Stieglitz, J., Curry, W. B. & Slowey, N. Weaker Gulf stream in the Florida Straits during the Last Glacial Maximum. *Nature* **402**, 644–648 (1999).
29. Weaver, A. J., Saaenko, O. A., Clark, P. U. & Mitrovica, J. X. Meltwater pulse 1A from Antarctica as a trigger of the Bolling/Allerod warm interval. *Science* **299**, 1709–1713 (2003).
30. Knorr, G. & Lohmann, G. Southern Ocean origin for the resumption of Atlantic thermohaline circulation during deglaciation. *Nature* **424**, 532–536 (2003).

Supplementary Information accompanies the paper on [www.nature.com/nature](http://www.nature.com/nature).

**Acknowledgements** We thank the Ocean Drilling Program (ODP) and the LDEO Deep-Sea Sample Repository for core samples. Laboratory assistance from D. Pak and mass spectrometer operation by G. Paradis and D. Winter were critical to the success of this study. We also thank A. Droxler for providing a suite of his ODP 999A samples, and J. Kennett and A. Russell for their comments and suggestions. Funding for this research was provided by a USSSP Schlanger Ocean Drilling Fellowship to M.W.S. and the US National Science Foundation (H.J.S. and D.W.L.).

**Competing interests statement** The authors declare that they have no competing financial interests.

**Correspondence** and requests for materials should be addressed to M.W.S. ([schmidt@geology.ucdavis.edu](mailto:schmidt@geology.ucdavis.edu)).

.....

## Seismic reflection imaging of two megathrust shear zones in the northern Cascadia subduction zone

Andrew J. Calvert

Department of Earth Sciences, Simon Fraser University, 8888 University Drive, Burnaby, British Columbia, V5A 1S6, Canada

At convergent continental margins, the relative motion between the subducting oceanic plate and the overriding continent is usually accommodated by movement along a single, thin interface known as a megathrust<sup>1</sup>. Great thrust earthquakes occur on the shallow part of this interface where the two plates are locked together<sup>2</sup>. Earthquakes of lower magnitude occur within the underlying oceanic plate, and have been linked to geochemical dehydration reactions caused by the plate’s descent<sup>3–7</sup>. Here I present deep seismic reflection data from the northern Cascadia subduction zone that show that the inter-plate boundary is up to 16 km thick and comprises two megathrust shear zones that bound a >5-km-thick, ~110-km-wide region of imbricated crustal rocks. Earthquakes within the subducting plate occur predominantly in two geographic bands where the dip of the plate is inferred to increase as it is forced around the edges of the imbricated inter-plate boundary zone. This implies that seismicity in the subducting slab is controlled primarily by deformation in the upper part of the plate. Slip on the shallower megathrust shear zone, which may occur by aseismic slow slip, will transport crustal rocks into the upper mantle above the subducting oceanic plate and may, in part, provide an explanation for the unusually low seismic wave speeds that are observed there<sup>8,9</sup>.

The Cascadia subduction zone, where the oceanic Juan de Fuca plate descends beneath the overlying North American plate, extends 1,100 km from northern California to northern Vancouver Island. Sedimentary rocks originally deposited on the oceanic plate are

scraped off and accreted to the western edge of the continent; the initiation of this process is indicated by the deformation front in Fig. 1. The intersection of the deformation front with the southwest-trending Nootka transform fault, which is characterized by high levels of seismicity, marks the approximate northern limit of the subduction zone. Beneath the western and eastern edges of Vancouver Island, earthquakes within the oceanic plate occur in two well-defined, ~50-km-wide, geographic bands that merge further south. These earthquakes have been attributed to dehydration embrittlement of the oceanic mantle<sup>7</sup> and the gradual transformation of basalt to eclogite<sup>6,7</sup>; this latter process may begin at depths as shallow as 40 km (ref. 6).

West of Vancouver Island, seismic refraction and normal incidence reflection surveys show that the top of the subducting oceanic crust lies immediately beneath a seismic reflector that dips landward at between 12 and 25 km depth<sup>10,11</sup> ('JdF' in Figs 2a and 3). Beneath southern Vancouver Island and its margins, seismic reflection surveys also identify two regionally extensive structures: a thick zone of reflectors, denoted by the letter E, and a deeper, probably individual, reflector, identified by the letter F (refs 12–15). On a composite reflection section across the northern Cascadia forearc (Fig. 2a), the E zone appears as a sequence of anastomosing reflections that extends over 1.0 to 3.2 s (corresponding to a thickness of 3–10 km), dips at 4–15°, and reaches a depth of at least 45 km east of Vancouver Island. The second reflection, F, is observed intermittently, between ~0.5 and 2.0 s (~2–6 km) later than the deepest reflector of the E sequence. The short duration of this reflection implies that it originates either from a thin, <2-km-thick, region, or at a single interface.

In offshore surveys, the F reflection can be traced seaward and upward towards the reflection from the top of the subducting plate west of Vancouver Island. As the F reflection shallows it approaches to within 0.5 s (<2 km) of the deepest of the E reflections, defining a wedge-like geometry (Fig. 2b). If the top of the subducting plate were located at the base of the E reflectors, then the most plausible interpretation of the F reflector would be as the oceanic Moho<sup>16</sup>, implying that the descending oceanic crust is <2 km thick in places. However, this conclusion is inconsistent with observations in the deep ocean basin where the Moho of the incoming oceanic plate is observed 1.8–2.2 s after the top of the igneous crust<sup>17</sup>. In fact, the Moho of the subducting plate is located by wide-angle reflections<sup>7</sup> recorded in the SHIPS<sup>18,19</sup> survey and occurs ~6 km deeper than the F reflector (Fig. 2b), consistent with modelling of gravity data<sup>20</sup> and analysis of teleseismic P to S wave conversions recorded near central Vancouver Island<sup>21</sup>. I therefore interpret the F reflector to be the top of the subducting plate.

The E reflections dip shallowly to the east-northeast (ENE) at approximately 4° across southern Vancouver Island. As the reflections reach the eastern edge of the island, their dip increases sharply to ~15° and they continue into the uppermost mantle with this dip. In contrast, the F reflection from the top of the subducting plate dips to the ENE at ~15° near the western edge of Vancouver Island, and then flattens out further to the east. It is not possible to identify unequivocally the shorter F reflection segments near the east coast of Vancouver Island owing to elevated levels of coherent noise; however, it seems unlikely that the F reflection would crosscut the E reflections. Therefore the F reflector must also increase in dip as it presumably merges into the deepest of the E reflectors near the eastern edge of Vancouver Island. Thus identified, the E and F reflectors define a ~110-km-wide duplex structure: the F reflection, which marks the top of the subducting plate, is the floor thrust with a ramp-flat-ramp geometry, and the E reflectors form a vertically distributed roof thrust (Fig. 4). In the region bounded by the E and F reflectors, P wave velocities (derived by three-dimensional (3D) tomographic inversion of first arrivals from local earthquakes and first arrivals of the SHIPS survey<sup>9</sup>) vary laterally between 6,800 and 7,200 m s<sup>-1</sup> (Fig. 2b). These velocity values are consistent with

crustal rocks of both the oceanic plate and the lower continental plate.

Earthquake hypocentres relocated as part of the 3D tomographic inversion<sup>9</sup> can be correlated accurately with the seismic reflection data and a corresponding vertical section extracted from the 3D velocity model. Earthquakes that occurred within 15 km of the seismic profiles have been projected laterally onto the profile and are shown in Fig. 2b, in which the reflection section has been converted to depth. The depth conversion used the extracted velocity model extended seaward with a combination of refraction velocities<sup>10</sup> and stacking velocities from the reflection profile<sup>22</sup>, and removed the effects on deep reflectors of lateral velocity variations in the near-surface. Earthquakes can be divided into two main groups, upper and lower, depending on whether they are above or below the E reflectors, which appear to be notably aseismic<sup>16</sup>.

Earthquakes occur above the E reflectors to depths as great as 35 km, but the seismicity terminates abruptly at the shallowest of the E reflectors. This distribution of earthquakes suggests that the region of the lower continental crust in which the E reflectors are located either cannot sustain stress accumulation or is completely locked; the latter is unlikely given an estimated temperature at the E reflectors of ~400 °C (ref. 23). Landward of the locked part of the inter-plate boundary, which extends landward 60 km from the deformation front<sup>2</sup>, accumulating stress is released through episodic, aseismic slow-slip events<sup>24</sup>. Simultaneous non-volcanic tremors<sup>25</sup> have been approximately located at multiple depths over at least 15 km above the subducting plate<sup>26</sup>. The existence of tremors at depths corresponding to the E reflectors, and the absence of conventional seismicity within the E reflectors, imply that slow slip is occurring here. Tremors occur at depths corresponding to the F reflector, suggesting that slip is also occurring at the top of the subducting plate. With the roof thrust of the duplex active, the

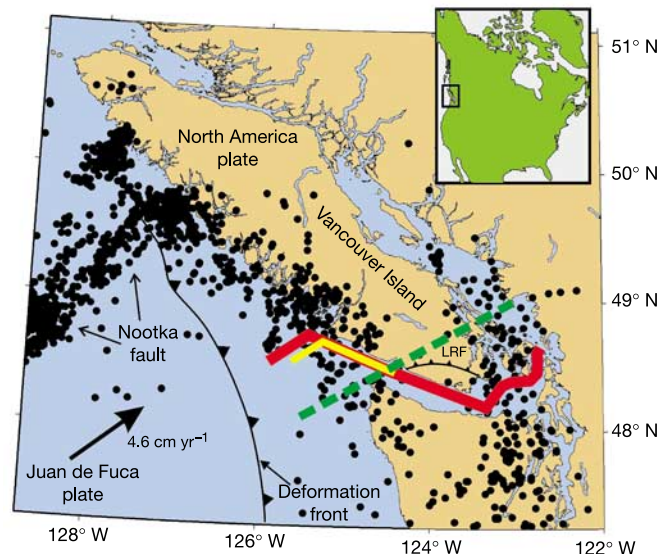


**Figure 1** Map of the northern Cascadia subduction zone showing the distribution of in-slab earthquakes (filled black circles) along the margin. The approximate northern limit of the Cascadia subduction zone is marked by the intersection of the deformation front with the Nootka fault, which is characterized by high levels of seismicity caused by relative motion between the Juan de Fuca plate and a small oceanic plate to the north. Earthquakes within the subducting slab occur predominantly along the western and eastern edges of Vancouver Island. The seismic lines combined to form the cross-section across the forearc region in Fig. 2 are shown in red, the azimuth of the simulated cross-section in green (dashed). The lines combined to form the section in Fig. 3 are shown in yellow. LRF, Leech River fault.

enclosed imbricated rocks will be transported downward (Fig. 4), perhaps into the forearc upper mantle, and this process may provide an explanation for the P wave velocities as low as  $6,800 \text{ m s}^{-1}$  that have been observed there<sup>8,9</sup>.

Near the west coast of Vancouver Island, numerous earthquakes, with a variety of focal mechanisms<sup>27</sup>, occur beneath the top of the subducting oceanic crust where it dips most steeply; only one earthquake occurs above the top of the plate, being located in the imbrication enclosed within the duplex structure (Figs 2b, 3). As the top of the plate flattens, the number of earthquakes within the slab

decreases markedly even though dehydration of the crust should be occurring here<sup>6</sup>. As indicated in Fig. 1, there is another belt of inslab earthquakes near the east coast of Vancouver Island, and Fig. 2b shows that this belt corresponds to the location where the inferred dip of the subducting plate increases once more. I propose that the two belts of inslab seismicity (Fig. 1) are due either to flexure or to fragmentation of the oceanic plate as it subducts obliquely around the edges of the imbricated inter-plate boundary zone (Fig. 4). Dehydration reactions may reduce the effective normal stresses across faults<sup>7</sup> and facilitate rupture when the subducting plate

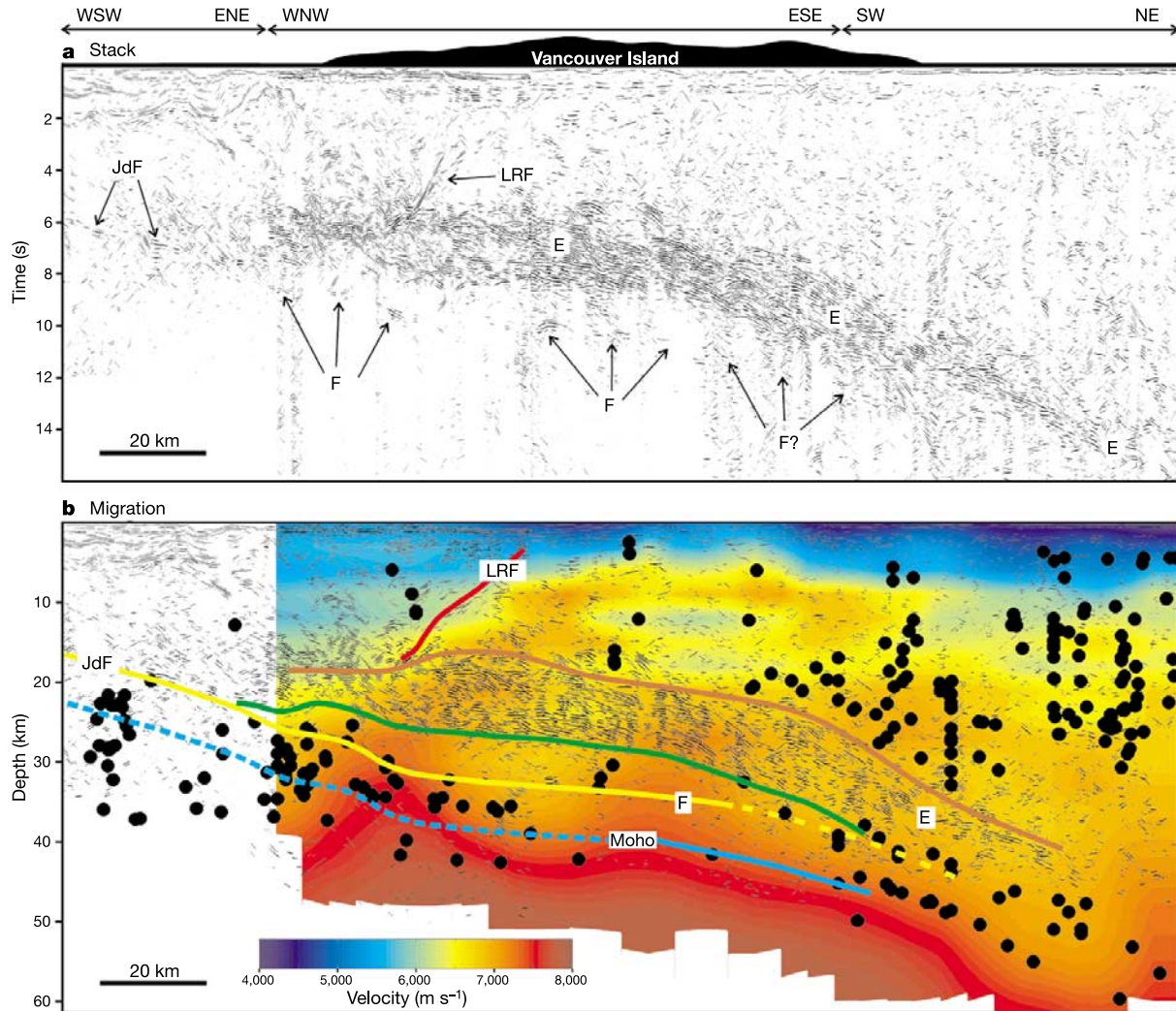


**Figure 2** Composite seismic cross-section across the Cascadia forearc region in the vicinity of southern Vancouver Island. **a**, Unmigrated section showing the reflection, labelled JdF, from the top of the subducting Juan de Fuca plate west of Vancouver Island, the E reflection zone, and the F reflection which marks the top of the subducting Juan de Fuca plate further east. Reflections from the Leech River crustal fault, LRF, are truncated by the E reflections. The lack of continuity of the F reflector beneath the western half of Vancouver Island is largely due to the gain used for this display; on higher-gain displays, the F reflector is continuous over ~80% of the profile with breaks attributable to localized variations in near-surface basement topography. The cross-section was constructed by projecting individual seismic profiles onto an azimuth of  $063^\circ$ , which is a representative dip direction for the subducting plate near the seismic profiles. The apparent dips of reflections such as JdF, E and F, which dip shallowly in directions close to the projection azimuth, are close to true dip on the simulated section. The orientation of the original line segments used to construct the composite section are shown at the top. **b**, Migrated section superimposed on a display of P wave velocities derived by 3D tomographic

inversion of first arrivals from local earthquakes and wide-angle airgun shots around Vancouver Island<sup>9</sup>. The velocities were extracted from the 3D velocity model along the composite seismic profile shown by the red line in Fig. 1 and projected in the same way as the seismic reflection data. Earthquakes, which were relocated in the tomographic inversion, are shown by filled black circles. The near-linear alignment of east-dipping inslab earthquakes just above the oceanic Moho at 45–55 km depth may indicate delamination of the oceanic crust. Steeply dipping seismic reflectors oblique to the line of projection may be mispositioned; however, for the shallowly ~ENE-dipping reflectors interpreted here, any lateral positioning errors will probably be of the order of the accuracy of the hypocentre locations and the cell size used in the tomographic inversion, namely 3 km, or less. Oceanic Moho constrained by wide-angle reflections, blue; oceanic Moho assuming subducting crust is 6 km thick, dashed blue; top of subducting plate, yellow; deepest E reflection, green; shallowest E reflection, brown; Leech River fault, red. Vertical exaggeration is 1.5:1.

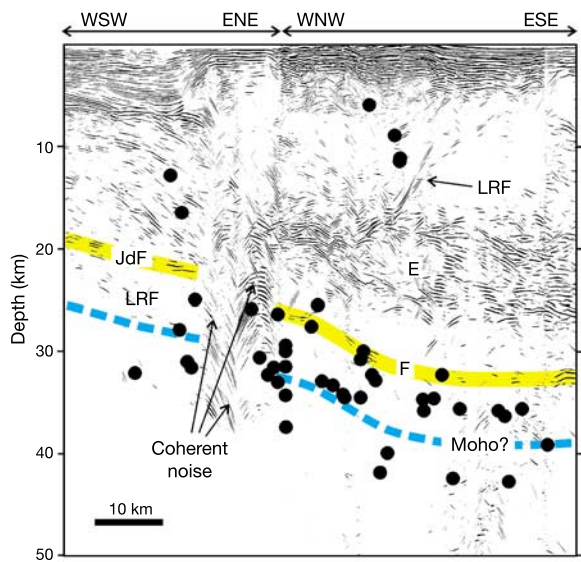


**Figure 3** Composite seismic section near the west coast of Vancouver Island. The shallowest of the inslab earthquakes follow the geometry of the top of the subducting Juan de Fuca plate (yellow line). Inslab earthquakes occur predominantly where the dip of the subducting plate increases to 15°, and infrequently elsewhere. Earthquake hypocenters within 15 km of the seismic profiles are shown by black filled circles. The seismic data are unmigrated, but the position of the top of the plate is derived from a migrated section, indicating that the position of the interface does not move a great distance after migration owing to its relatively low dip. The orientation of the original line segments used to construct the composite section are shown at the top. Oceanic Moho assuming subducting crust is 6 km thick, dashed blue line. Vertical exaggeration is 1.5:1.

flexes, for example, near the west coast of Vancouver Island. At the eastern edge of Vancouver Island, the oceanic crust reaches 40 km depth where the transformation of basalt to eclogite begins<sup>6</sup>, and focal mechanisms are dominated by downdip tension<sup>27</sup>. The consequent increase in density of the crust may facilitate the sudden increase in dip of the subducting slab here, and perhaps result in delamination of the crust, as suggested by an alignment of earthquake hypocentres just above the oceanic Moho (Fig. 2b).

The two seismic belts (Fig. 1) may indicate the lateral extent of the imbricated zone between the E and F reflectors, implying that most of southern Vancouver Island is underlain by a ~110-km-wide duplex structure, an order of magnitude greater than lenses of sediment that can be eroded from the base of accretionary wedges beneath the continental slope<sup>28</sup>. Within the imbricated zone, a few earthquakes occur where P wave velocities change laterally, suggesting that these earthquakes might be attributable to imbricate thrusting that has juxtaposed different lithologies. If these imbricated rocks are derived mostly from the forearc, then the duplex may result from erosion of the lower crust, perhaps below shelf basins where high inter-plate coupling has been proposed<sup>29</sup>. Alternatively, if the imbricated rocks originated in the oceanic plate, they would be underplated to the North American plate should aseismic slip along the E reflectors cease, and reorganization of faults within the duplex occur. If slip along the F reflector were to cease, the duplex would become welded to the downgoing slab, and thickened crust would be subducted, as proposed for the Yakutat terrane in Alaska<sup>30</sup>.

Subduction is usually viewed as occurring along a single, thin interface beneath which an oceanic plate descends into the mantle, and inslab seismicity is considered to be driven by dehydration metamorphism<sup>3–7</sup>. In the northernmost Cascadia subduction zone, however, the inter-plate boundary is a complex zone up to 16 km in

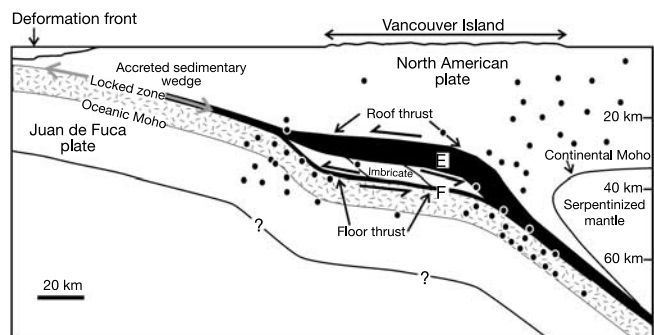


**Figure 4** Schematic cross-section of the northern Cascadia convergent margin at southern Vancouver Island. The plate boundary forms a thick duplex structure, within which crustal rocks are imbricated. Inslab earthquakes occur where the dip of the top of the subducting slab, which defines the floor thrust, increases suddenly, suggesting that the earthquakes are caused by deformation in the upper part of the subducting slab as it responds to the geometry of the inter-plate boundary zone. The E reflectors form the roof thrust, and are probably one location of the aseismic, slow-slip events. Slip along the roof thrust will transport the imbricated crustal rocks into the upper mantle above the subducting oceanic slab. Slow slip is also probably occurring along the floor thrust, which is inferred to be the top of the subducting plate. Earthquake hypocentres are indicated by black circles. Vertical exaggeration is 1.5:1.

vertical extent, and inslab seismicity is controlled by deformation in the upper part of the subducting plate. □

Received 11 October 2003; accepted 28 January 2004; doi:10.1038/nature02372.

1. Rogers, G. C. An assessment of the megathrust earthquake potential of the Cascadia subduction zone. *Can. J. Earth Sci.* **26**, 844–852 (1988).
2. Hyndman, R. D. & Wang, K. The rupture zone of Cascadia great earthquakes from current deformation and the thermal regime. *J. Geophys. Res.* **100**, 22133–22154 (1995).
3. Kirby, S. H. *et al.* in *Subduction: Top to Bottom* (ed. Bebout, G. E.) 195–214 (American Geophysical Union, Washington DC, 1996).
4. Peacock, S. M. & Wang, K. Seismic consequences of warm versus cool subduction metamorphism: Examples from southwest and northeast Japan. *Science* **286**, 937–939 (1999).
5. Peacock, S. M. Are the lower planes of double seismic zones caused by serpentine dehydration in subducting oceanic mantle? *Geology* **29**, 299–302 (2001).
6. Hacker, B. R., Peacock, S. M., Abers, G. A. & Holloway, S. D. Subduction factory 2. Are intermediate-depth earthquakes linked to metamorphic dehydration reactions? *J. Geophys. Res.* **108**, doi:10.1029/2001JB001129 (2003).
7. Preston, L. A., Creager, K. C., Crosson, R. S., Brocher, T. M. & Tréhu, A. M. Intraslab earthquakes: Dehydration of the Cascadia slab. *Science* **302**, 1197–1200 (2003).
8. Stanley, D., Villasenor, A. & Benz, H. *Subduction Zone and Crustal Dynamics of Western Washington: A Tectonic Model for Earthquake Hazards Evaluation* Open File Report 99–311 (US Geological Survey, Reston, 1999).
9. Ramachandran, K. *Velocity Structure of S.W. British Columbia and N.W. Washington from 3-D Non-linear Seismic Tomography* Thesis, Univ. Victoria (2001).
10. Spence, G. D., Clowes, R. M. & Ellis, R. M. Seismic structure across the active subduction zone of western Canada. *J. Geophys. Res.* **90**, 6754–6772 (1985).
11. Clowes, R. M., Yorath, C. J. & Hyndman, R. D. Reflection mapping across the convergent margin of western Canada. *Geophys. J. R. Astron. Soc.* **89**, 79–84 (1987).
12. Green, A. G. *et al.* Seismic reflection imaging of the subducting Juan de Fuca plate. *Nature* **319**, 210–213 (1986).
13. Clowes, R. M. *et al.* LITHOPROBE—southern Vancouver Island: Cenozoic subduction complex imaged by deep seismic reflections. *Can. J. Earth Sci.* **24**, 31–51 (1987).
14. Calvert, A. J. & Clowes, R. M. Deep, high-amplitude reflections from a major shear zone above the subducting Juan de Fuca plate. *Geology* **18**, 1091–1094 (1990).
15. Calvert, A. J. Seismic reflection constraints on imbrication and underplating of the northern Cascadia convergent margin. *Can. J. Earth Sci.* **33**, 1294–1307 (1996).
16. Nedimović, M. R., Hyndman, R. D., Ramachandran, K. & Spence, G. D. Reflection signature of seismic and aseismic slip on the northern Cascadia subduction interface. *Nature* **424**, 416–420 (2003).
17. Hasselgren, E. O. & Clowes, R. M. Crustal structure of northern Juan de Fuca plate from multichannel seismic reflection data. *J. Geophys. Res.* **100**, 6469–6486 (1994).
18. Fisher, M. A. *et al.* Seismic survey probes urban earthquake hazards in Pacific Northwest. *Eos* **80**, 16–17 (1999).
19. Brocher, T. M. *et al.* *Wide-angle Seismic Recordings from the 1998 Seismic Hazards Investigation in Puget Sound (SHIPS)*, Western Washington and British Columbia Open File Report 99–314 (US Geological Survey, Reston, 1999).
20. Dehler, S. A. & Clowes, R. M. Integrated geophysical modelling of terranes and other structures along the western Canadian margin. *Can. J. Earth Sci.* **29**, 1492–1508 (1992).
21. Cassidy, J. F. & Ellis, R. M. Shear wave constraints on a deep crustal reflective zone beneath Vancouver Island. *J. Geophys. Res.* **96**, 19843–19851 (1991).

22. Yorath, C. J. *et al.* *Marine Multichannel Seismic Reflection, Gravity and Magnetic Profiles—Vancouver Island Continental Margin and Juan De Fuca Ridge* (Open File Report 1661, Geological Survey of Canada, Vancouver, 1987).

23. Hyndman, R. D. Dipping reflectors, electrically conductive zones and free water beneath a subduction zone. *J. Geophys. Res.* **93**, 13391–13405 (1988).

24. Dragert, H., Wang, K. & James, T. S. A silent slip event on the deeper Cascadia subduction interface. *Science* **292**, 1525–1528 (2001).

25. Rogers, G. & Dragert, H. Episodic tremor and slip on the Cascadia subduction zone: The chatter of silent slip. *Science* **300**, 1942–1943 (2003).

26. Kao, H., Shan, S.-J., Rogers, G., Cassidy, J. F. & Dragert, H. Temporal and spatial distribution of the tremors in the episodic tremor and slip (ETS) event observed beneath the northern Cascadia subduction zone in early 2003. *Eos* **84** (Fall Meeting Suppl.), S42G–02 (2003).

27. Bolton, M. K. & Rogers, G. C. Juan de Fuca plate seismicity at the northern end of the Cascadia subduction zone. *Seismol. Res. Lett.* **73**, 214 (2002).

28. Ranero, C. R. & von Huene, R. Subduction erosion along the Middle America convergent margin. *Nature* **404**, 748–752 (2003).

29. Wells, R. E., Blakely, R. J., Sugiyama, Y., Scholl, D. W. & Dinterman, D. A. Basin-centered asperities in great subduction zone earthquakes: A link between slip, subduction and subduction erosion. *J. Geophys. Res.* **108**, doi:10.1029/2002JB002072 (2003).

30. Brocher, T. M., Fuis, G. S., Fisher, M. A., Plafker, G. & Moses, M. J. Mapping the megathrust beneath the northern Gulf of Alaska using wide-angle seismic data. *J. Geophys. Res.* **99**, 11663–11685 (1994).

**Acknowledgements** I thank K. Ramachandran for making available to me the 3D velocity model and the positions of the relocated earthquakes; T. Brocher for comments and suggestions that helped to improve the final manuscript; and H. Kao and M. Nedimović for discussions. This project was funded by the Natural Sciences and Engineering Research Council of Canada.

**Competing interests statement** The author declares that he has no competing financial interests.

**Correspondence** and requests for materials should be addressed to the author (acalvert@sfu.ca).

## Unified spatial scaling of species and their trophic interactions

Ulrich Brose<sup>1,2\*</sup>, Annette Ostling<sup>3</sup>, Kateri Harrison<sup>2</sup> & Neo D. Martinez<sup>2</sup>

<sup>1</sup>Department of Computer Science, Thorton Hall 906, 1600 Holloway Avenue, San Francisco State University, San Francisco, California 94132-4163, USA

<sup>2</sup>Pacific Ecoinformatics and Computational Ecology Laboratory, Rocky Mountain Biological Laboratory, POB 519, Gothic, Colorado 81224, USA

<sup>3</sup>Energy and Resources Group, University of California, Berkeley, California 94720-3050, USA

\* Present address: Technical University of Darmstadt, Department of Biology, Schnittspahnstr. 3, D-64287, Darmstadt, Germany

Two largely independent bodies of scaling theory address the quantitative relationships between habitat area, species diversity and trophic interactions. Spatial theory within macroecology addresses how species richness scales with area in landscapes, while typically ignoring interspecific interactions<sup>1–6</sup>. Complexity theory within community ecology addresses how trophic links scale with species richness in food webs, while typically ignoring spatial considerations<sup>7–12</sup>. Recent studies suggest unifying these theories by demonstrating how spatial patterns influence food-web structure<sup>13–16</sup> and vice versa<sup>17</sup>. Here, we follow this suggestion by developing and empirically testing a more unified scaling theory. On the basis of power-law species–area relationships, we develop link–area and non-power-law link–species models that accurately predict how trophic links scale with area and species richness of microcosms, lakes and streams from community to metacommunity levels. In contrast to previous models that assume that species richness alone determines the number of trophic links<sup>7,8</sup>, these models include the species’ spatial distribution, and hence extend the domain of complexity theory to metacommunity scales. This generality and predictive success shows how complexity theory and spatial theory can be unified into a much more general theory addressing new domains of ecology.

A widely observed pattern in ecology is the power-law scaling of the number of species  $S$  of a metacommunity with local habitat area  $A$

$$S = cA^z \quad (1)$$

where  $c$  and  $z$  are positive constants<sup>1,2</sup>. This relationship may occur when colonization frequency increases with area and extinctions become less likely in larger habitats because of larger populations<sup>1–3</sup>, in which case spatial isolation can reduce  $z$  by preventing colonization events<sup>1–3</sup>. A recent incorporation of trophic considerations into spatial scaling theory suggests that  $z$  increases with trophic level<sup>17</sup>. Here, we reinforce this bridge between fields in the opposite direction by incorporating spatial scaling considerations into trophic theory.

Theories of biocomplexity within local communities express the power-law scaling of feeding links between species,  $L$ , with species richness,  $S$ , as

$$L = bS^u \quad (2)$$

where  $b$  and  $u$  are positive constants<sup>7–10</sup>. The ‘link–species scaling law’ asserts that consumers have a finite number of resources that is independent of community diversity ( $u = 1$ )<sup>7</sup>. The alternative ‘constant connectance hypothesis’ asserts that species are linked on average to a fixed fraction of other species, and that links scale with the square of species richness ( $u = 2$ )<sup>8</sup>. Empirical analyses find exponents spanning this range ( $1 \leq u \leq 2$ )<sup>7–10</sup> and classical stability theory predicts exponents at the low end of this range due to positive feedbacks thought to accompany higher linkage densities<sup>18</sup>. However, spatial patterns may ameliorate this instability of highly diverse food webs<sup>16,18–20</sup>. A few studies have found that ecosystem size determines the length of food chains<sup>14–16</sup>, but such study of the effects of space on food-web structure is surprisingly limited. Here, we address this limitation by deriving link–area and spatially explicit link–species relationships from species–area models and testing them against the best available data.

Combining equations (1) and (2) yields a simple model for the scaling of links with area

$$L = bc^u A^{uz} \quad (3)$$

This link–area relationship depends on whether the link–species scaling law ( $u = 1$ )<sup>7</sup> or the constant connectance hypothesis ( $u = 2$ )<sup>8</sup> is accepted. Being based on equation (2), equation (3) also assumes that the link–species relationship in equation (2) holds independent of the value of  $S$ . This characterizes local communities, in which all  $S$  species co-occur spatially and therefore all consumers co-occur with and consume their resources among the  $S$  species<sup>8</sup>. In metacommunities, species may be spatially isolated from potential consumers and resources, which might prevent certain links from being realized<sup>8</sup>. This suggests that equations (2) and (3) inaccurately predict trophic complexity at macroecological scales<sup>8,21</sup>. Here, we address this potential inaccuracy by starting with the species–area model in equation (1) and deriving the following food-web complexity models, which do not assume general consumer–resource co-occurrence (see Box 1):

$$L = K\theta(A)A^{2z} = (K/c^2)\theta(A)S^2 \quad (4)$$

$$L = K\theta(A)A^{z_k+z_r} = \frac{K}{c_k c_r} \theta(A) S_k S_r = \frac{K}{c_k c_r} \theta(A) S^u \quad (5)$$

where  $K$  is constant. In contrast to equation (4), equation (5) accounts for differences in the species–area relationships between consumers and resources, as indicated by the subscripts  $k$  and  $r$ , respectively.  $\theta(A)$  represents the increased or decreased likelihood of consumer species occurrences in patches with their resources compared with random patches. This effectiveness of consumers tracking their resources may be scale dependent. For the metacommunity in area  $A_0$ ,  $L(A_0) = L_0$  if  $\theta(A_0) = 1$ . At other spatial scales,  $\theta(A) > 1$  or  $\theta(A) < 1$  indicates that, on average, consumer species